MULTI-ROTOR WAKE INTERACTION CHARACTERIZATION

F. De Gregorio, Italian Aerospace Research Centre - CIRA, Capua, Italy
K.-S. Rossignol, DLR, Braunschweig, Germany
G. Ceglia, Italian Aerospace Research Centre - CIRA, Capua, Italy
J. Yin, DLR, Braunschweig, Germany

Abstract

The paper presents part of the experimental activities carried out in the GARTEUR Action Group HC/AG-26 to study the acoustic and aerodynamic characteristics of small rotor configurations, including the influence of the rotor-rotor interactions. Two rotors equipped with two-bladed propellers with a diameter of D=165.1mm were used at two different rotating speeds of 8025 RPM and 10120 RPM and different geometry configurations. Isolated rotor and coaxial configurations in hover conditions were assessed. The rotor slipstream characterization, in terms of aerodynamic loads, flow field velocity and acoustics emissions, was performed using a six-component load cell, Particle Image Velocimetry and microphone array measurements. The effect of the rotor support/fairing on the performance of the isolated rotor was investigated together with the rotor-rotor interaction for the coaxial configuration at two rotor distances of Δz = 0.5R and Δz = 1.0 R. The results indicated an effect of the support/fairing on the propeller performance, a loss of thrust of the lower rotor and a higher noise emission for the coaxial configuration characterized by the larger rotor distance. The turbulent kinetic energy and the meandering of the blade tip vortices sustained the acoustics results.

1 NOMENCLATURE

Symbol	Description	Units
c	Chord length	m
D	Rotor diameter	m
r	Local radius	m
R	Rotor radius	m
t	Time	s
V_{Tip}	Blade tip speed ($= \Omega R$)	m/s
V_θ	Swirl (tangential) velocity	m/s
V_x, V_y, V_z	Velocity components	m/s
x, y, z	Geometrical coordinates	m
$\Delta x, \Delta y$	Space resolution	mm
ζ_i	Wake age of blade # i	deg
θ	Blade twist	deg
σ	Rotor solidity	
ω_y	Out-of-plane vorticity	$1/s$
ψ	Blade azimuth angle	deg
ψ_{vi}	Tip Vortex age of blade # i	deg
Ω	Rotor speed	RPM

2 INTRODUCTION

Efforts in the development of aerial vehicles for Urban Air Mobility (UAM) to face congestion problems due to city transportation paved the way for unveiling their aerodynamic and acoustic characteristics [1], [2]. Multirotor propulsion systems are increasingly applied as suitable arrangements in Vertical Take-Off and Landing (VTOL) configurations. Multirotor systems become popular for small-scale drones, making them useful for a variety of tasks, i.e., surveillance, monitoring, searching, aerial surveying and photography. In this context, the GARTEUR Action Group HC/AG-26 [3] has been established to improve the current knowledge about rotor interaction; the project team comprises the participation of 14 partners coordinated by DLR. The main objectives of this AG are (1) to gain knowledge in noise generation and noise propagation of multirotor systems under the influence of the installation effects and (2) to develop and validate numerical prediction methods for the noise prediction for multirotor systems. The code validations are assessed by sharing among all the participants the experimental results gathered by the partner, deputed for the conduction of the test campaigns. Three test databases were available, which are from DLR [4][5], CIRA/CUSANO [6][7] and PoliMi [8].

Accordingly, CIRA and DLR carried out the first joint test campaign, using DLR multi-rotor test rig [4][5]. This foresaw particle image velocimetry (PIV) flow field measurements of the rotor slipstreams

Presented at 49th European Rotorcraft Forum, Buckeburg, Germany, 5-7 September, 2023

performed in different configurations, i.e., the baseline cases considering isolated rotors and either coaxial arrangements placing them at two different vertical distances, Δz = 0.5 R or Δz = 1.0 R, between each other. Simultaneously, the aerodynamic characterization was carried out for all the test cases using a six-components load cell. These data integrate the acoustic measurements conducted at the same test conditions in the Acoustic Wind Tunnel Braunschweig (AWB) [9]. Preliminary comparisons between numerical predictions and experimental data are presented by Yin et al [10].

The paper illustrates the experimental activities carried out on two different test campaigns, one performed at the DLR AWB facility and the second carried out at CIRA laboratories. The scope of the activities is focused on the multi-rotor characterization in terms of loads, velocity fields and acoustic emissions. The first part of the paper describes the main characteristics of the multi-rotor test rig, the experimental set-ups, the different rotor configurations and the selected test matrix. The study ends with the results related to the ensemble average velocity fields for isolated rotors and coaxial configurations, together with the load measurements concerning the effects due to the rotor interaction on the aerodynamic efficiency. PIV phase-locked measurements with flow characteristics related to different azimuth angles are discussed with flow vorticity behaviour, tip vortex detection and their main characteristics. The multi-rotor wake interaction is then discussed in terms of acoustic emission looking for possible relations between the different physical magnitudes.

3 EXPERIMENTAL SETUP

3.1 Rotor Rig

The rotor rig was originally designed to be used in the AWB [9]. Early investigations using the rig were conducted to acquire the acoustic emission characteristics of the selected rotors and configurations. The results of these investigations have been published by Rossignol et al. [4]. The AWB is DLR's small-size high-quality anechoic testing facility. It is an open-jet Göttingen-type wind tunnel capable of running at speeds of up to 65 m/s and optimized for noise measurements at frequencies above 250 Hz. The nozzle is 1.2 m high by 0.8 m in width. Special support was designed to extend the capabilities of the facility to meet the requirements of simultaneous measurements of multiple rotors under static and flight conditions, e.g. Figure 1.

Using this setup, several rotor configurations can be investigated; isolated, coaxial, and tandem with vertical and lateral offset. Rotors with a diameter of up to 0.4 m can be tested.

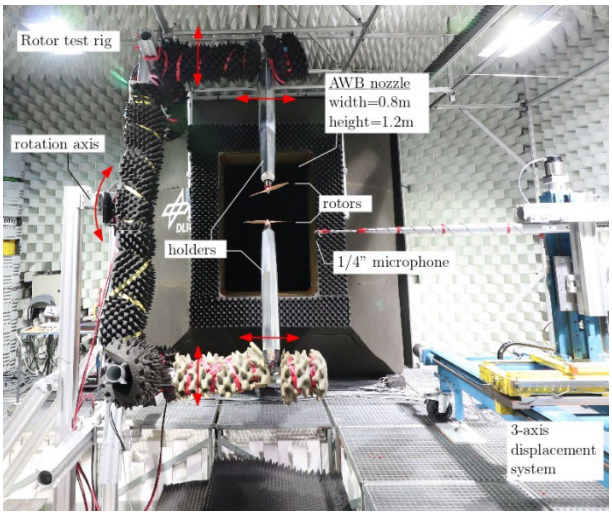

Figure 1: Rotor test rig at AWT

In this paper, we focus on data acquired with 13 inches diameter (D=330.2 mm) and 7 inches (177.8 mm) pitch beechwood rotors from the German small-scale propeller manufacturer Xoar Electric. The rotor has a solidity of σ=0.072 and the blade is characterised by a mean chord length $c = 18.7mm$. Blade geometry airfoil and propeller details in terms of chord, thickness and twist distribution along the radius are given in Figure 2.

The rotors are propelled by 14-poles Leopard LC5065 brushless motors with 0.2 mm stator plates and 520 U/min/V. Each motor is controlled by YGE 205HVT speed controllers, capable of a theoretical maximum speed of 34283 revolutions per minute (RPM), and SM300-Series 3300 W DC power supplies. The motors can deliver a maximum power of 2.1 kW. The power supplies allow a maximum tension of 30 V and correspondingly, a maximum current of 70 A. This combination allows RPM up to 13000 to be reached with an installed propeller. Without a mounted propeller, a maximum RPM of 15600 would be theoretically achievable. A Hall-effect RPM sensor is mounted on the motor's shafts to provide independent direct measurements of each motor's RPM. Both the RPM signal and the acoustic signals are acquired synchronously. This 1/rev signal also serves as a trigger signal for the acoustic data later in post-processing and synchronises the phase-locked PIV measurement system. The acquisition of the load signals is done synchronously with the acquisition of the microphone and Hall-effect sensor (RPM) signals at a sampling rate of 100 kHz.

For each rotor, performance data, in terms of thrust and torque, is acquired through miniature six-component load cells, Model K6D40 from ME-Meßsysteme GmbH Berlin Germany, mounted beneath the motors. To minimize the impact of temperature changes and electromagnetic fields from the motors on measurements, the load cells are

Presented at 49th European Rotorcraft Forum, Buckeburg, Germany, 5-7 September, 2023

isolated from the motors using an aluminium block spacer. The load cells are strain-gauge-based instruments which measure three orthogonal forces (F_x, F_y, F_z) and three orthogonal moments (M_x, M_y, M_z). The load cells were factory calibrated by the manufacturer to a full-scale thrust F_z=200 N (F_x=F_y=50 N) and a full-scale torque M_z=5 Nm. The load cell signals are sampled at a rate of 5 Hz by the pre-conditioning amplifier box. The manufacturer's data sheet rates the load cell with a precision (bias error) of 0.2 % full-scale. Preliminary investigations have shown that this value is dependent on temperature variations and is also RPM dependent, i.e. load dependent. A conservative estimate of the bias error on the load measurement is 0.5 % full-scale, though in the experiment this error was minimized through frequent zeroing of the load cells and short measurement durations

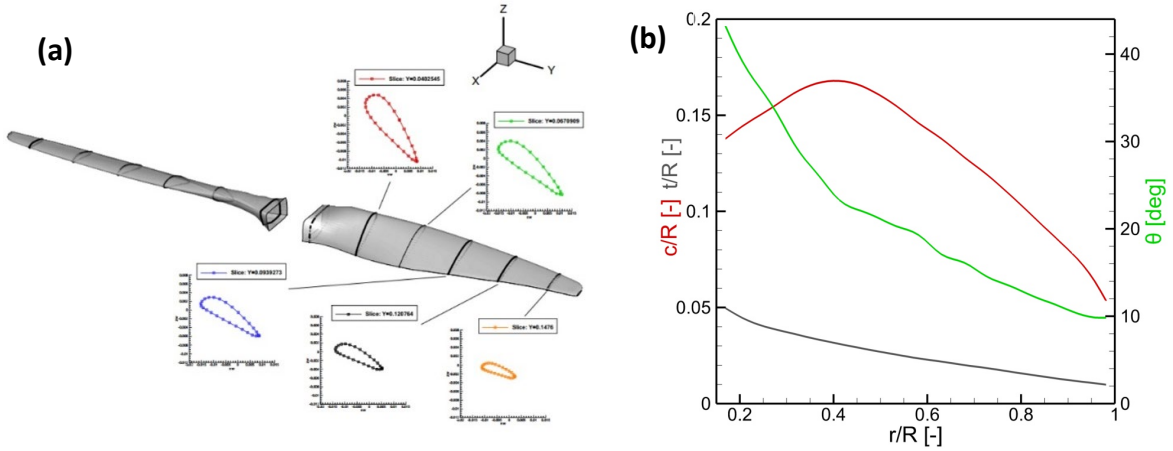

Figure 2: Propeller airfoil (a) and blade chord (red line), thickness (grey line) and twist (green line) radial distribution (b)

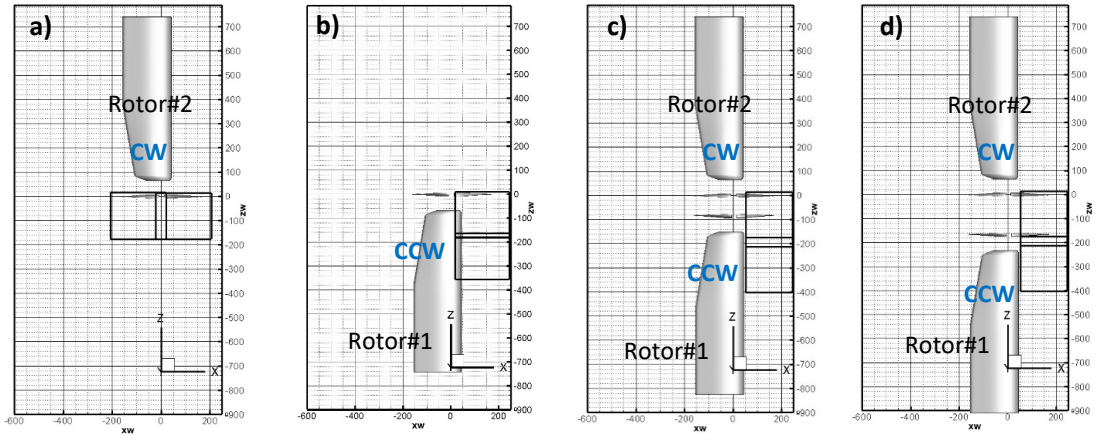

Figure 3: Different rotor rig layouts: Isolated rotor #2 (a); Isolated rotor #1 (b); Coaxial Δz = 0.5 R (c); Coaxial Δz = 1.0 R (d).

3.2 Rotor Rig Configurations and Reference System

The DLR test rig allows for testing different configurations, i.e., the isolated rotors, coaxial and tandem arrangements with a variety of parametric combinations. Among all the investigated combinations, however, the results pertaining to both isolated and coaxial configurations are reported herein. The isolated rotors present two different mounting concepts one is held from above (Figure 3-a), following an upside-down orientation, and the other is from below (Figure 3-b) named herein rotor #2 and rotor #1, respectively. Even though the different mounting features, both rotors revolve by generating up thrust hence, yielding the slipstreams flowing down. In turn, in rotor #1 the wake flow field impinges the fairing of the rotor; whereas, in rotor #2 it freely flows. The flow field and the aerodynamic performance were inspected for possible effects due to the fairing. The rotating versus of rotor #2 is clockwise for an observer looking from above while rotor #1 drives counterclockwise. The origin of the reference system is located in the centre of the rotor #2 rotating axes, the x-axis lays horizontal along the

Presented at 49th European Rotorcraft Forum, Buckeburg, Germany, 5-7 September, 2023

rotor blade, the z-axis is vertically and upward oriented and the y-axis follows the right-hand rule. Two coaxial configurations were investigated, the case characterized by a vertical distance between the rotor disk of Δz = 0.5 R of the blade radius (Figure 3-c) and at a larger distance of Δz = 1.0 R (Figure 3-d). All the configurations were investigated at rotating speeds of Ω=8025 RPM and Ω=10120 RPM corresponding to a Reynolds number ($Re_{75\%}$) based on the chord length at 75% of the blade radius of $1.4*10^5$ and $1.76*10^5$, respectively. To avoid wall interference, the rotor disks were positioned at a minimum distance from the ground and the ceiling of 4.1 and 4.0 blade diameters, respectively.

3.3 PIV measurement system

The rotor downwash characteristics were measured by a two-component Particle Image Velocimetry (2C-PIV) measurement system and by stereo PIV measurements.

The set-up was composed of a CFR 400 dual-head Nd-Yag laser with a pulse energy of E=200 mJ at a wavelength of λ=532nm and a repetition rate of 10Hz. A system of two sCMOS cameras was installed consisting of two ILA.PIV.sCMOS CLHS (25 frame rate, 2560×2160 pixels, 16-bit, pixel dimension 6.3 μm). To characterise the wake in the proximity to the rotor disk, the two sCMOS cameras were equipped with a Canon ES lens featuring a fixed focal length of f = 50 mm and the f-number was set to f# = 8. The lens focus distance and aperture were remotely controlled by the operators. The cameras were installed on a two axes linear traversing system, to increase the measured region by vertically shifting the cameras.

Different set-ups were arranged for the different rotor rig configurations. The rotor #2 wake investigation foresaw the installation side-by-side of two cameras horizontally oriented as shown in Figure 4-a. The measurement region was located immediately below the rotor disk plane on a vertical plane radially ranging between x/R = -1.3 and x/R = 1.2. The wake was measured along the axial direction between z = 0.02 R to z = -2.05 R, by stitching together the images the two cameras translated vertically of about one radius and partially overlapped.

The investigation of the isolated rotor #1 and the two coaxial configurations and the presence of the wind fairing below the rotor drove the installation of the two cameras side-by-side and vertically aligned to follow the wake evolution along the axial direction. The measured region of interest covers radially the wake in the range between x = 0.16 R to x = 1.3R and vertically from z = 0.16 R to z = -2.16 R.

This yielded a spatial resolution of about 11.3 px/mm in the image plane. The separation time between the laser double-pulses was set between 35 μs down to 25 μs according to the highest expected velocities in the flow. As tracer particles, aerosolized diethylhexylsebacate (DEHS) oil was used. A seeding generator with 20 Laskin nozzles provided oil droplets with a size of less than 1 μm. The full test room was seeded to have a homogenous concentration of particles. The PIV images were pre-processed by applying a background grey-level subtraction. PivView v3.6.5 (by PivTech GmbH) was used to process the particle images. The particle images analysis consisted of an iterative multigrid cross–correlation algorithm ending at 32x32 px^2 and 50% overlap.

The results presented a velocity spatial resolution of $\Delta x = 1.41mm$. The random noise of the PIV cross–correlation procedure can be estimated as 0.1 px as a rule–of–thumb (Raffel et al.[11]). Using the current values for the optical resolution (11.3 px/mm) and the laser double–pulse delay (25-35 μs), this is related to a velocity error of ΔV of ~ 0.25 m/s to 0.35 m/s.

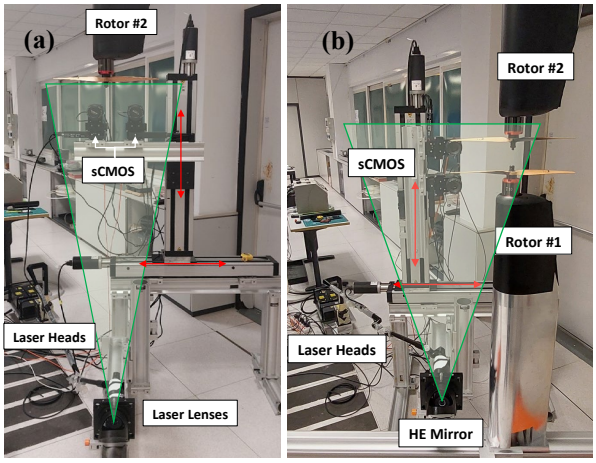

Figure 4: PIV experimental set-up: Isolated Rotor #2 wake characterization (a) and coaxial rotors investigations (b)

3.4 Acoustic measurement system

The rotor's acoustic emission was acquired through a single 1/4" GRAS 40 DP pressure field microphone mounted to a 3-axis linear displacement system (e.g. Figure 1). The microphone was placed in the flow field with its membrane protected by a Brüel und Kjær nose cap. The microphone was aligned parallel to the flow field with its sensing surface pointing upstream. The acoustic signal, along with the 1/rev signal, is sampled at a 100 kHz rate on a GMB Viper GmbH 48 channel data acquisition unit. The processing takes advantage of the 1/rev signal to phase-lock the data on a revolution-per-revolution basis before spectral and time domain analysis. Each data block is normalized to a unit revolution time to account for fluctuations in the total revolution sample count. The typical standard deviation of the sample count per revolution is on the order of 1 to 2 samples, i.e. 10 μs- 20 μs, depending on the configuration and

Presented at 49th European Rotorcraft Forum, Buckeburg, Germany, 5-7 September, 2023

RPM, with lower RPM showing smaller variations. At the operating speed of 8000 RPM, one revolution counts on average 748 samples, while at a rotating speed of 12000 RPM, this count is reduced to 500 samples. Before Fourier analysis, 32 individual blocks, i.e. revolutions, are stacked together to form a sufficiently long sequence to achieve a high-frequency resolution. Each time series is then Fourier transformed using a Hanning window to minimize spectral leakage issues. Averaged spectra are obtained through ensemble averaging of individual spectra and through time domain ensemble averaging prior to the Fourier analysis step. Spectral averaging preserves the broadband content of the signals, whereas time domain averaging tends to reduce it due to its incoherent nature and thus emphasizes the harmonic components.

4 RESULTS

4.1 Aerodynamic Results

The aerodynamic characteristics of either the isolated rotors were investigated varying the rotating speed in the range between 4000 RPM to 10500 RPM. The six components of the aerodynamic forces and moments were measured for all the cases. The forces and moments in the rotor disk were negligible while thrust F_z and torque M_z behaviour are shown in Figure 5.

Both rotors have a similar trend, increasing as a second-order law as the speed increases. Rotor #2 thrust behaviour presents a slightly higher value concerning rotor #1 for the full velocity range. At the two speeds of interest, 8025 RPM and 10120 RPM, the thrust increment is of about F_z = 2 N, corresponding to percentage values of 9% and 5%, respectively. The coaxial configuration depicts no effects on the thrust of the upper rotor, with the markers falling on the rotor #2 black solid line. A clear effect occurs on rotor #1, showing a sensitive decrement of the thrust for both coaxial configurations. The coaxial configuration characterised by a vertical distance of Δz=0.5R presents for both rotating speeds a percentage decrement of about 17% concerning the thrust of the isolated rotor #1, while the configuration with a vertical distance of Δz = 1 R exhibits a slightly larger loss of thrust of 18% and 19% at Ω=8025 RPM and Ω=10120 RPM, respectively.

Both rotor torque trends are similar, with rotor #2 characterized by a little higher value with respect the rotor #1. For rotor #2, both the coaxial configurations indicate no evident effect on the torque while rotor #1 presents slightly higher values with respect to the isolated rotor instead of lower values. This behaviour is probably due to different effective angles of attack and relative speed due to the incoming slipstream and it is worth to further investigation with the support of CFD investigation.

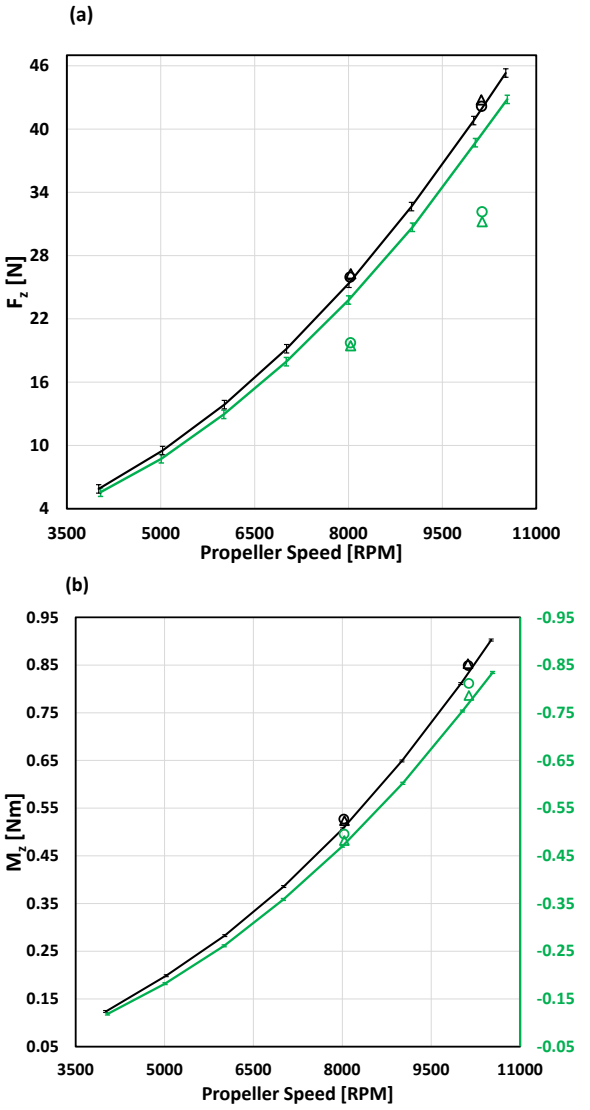

Figure 5: Thrust (a) and torque (b) of rotor #1 (in green) and #2 (in black) as a function of the rotor speed for the isolated (continuous lines) and co-axial configurations at Δz = 0.5 R (circles) and Δz = 1.0 R (triangles). The error bars indicate the standard deviation of the present dataset.

4.2 Ensemble Average Velocity Fields

PIV measurements were carried out to investigate the rotor slipstream characteristic for different rotor rig configurations. Ensemble average velocity fields were obtained on a set of five hundred instantaneous velocity fields gathered at different rotor azimuth angle positions. The rotating speeds were selected to avoid any lock between the acquisition frequency and the rotor speed. The slipstream of rotor #1 is confined by the presence of the wind fairing support (Figure 6 a and c) while the rotor #2 wake is free to develop being fixed from above (Figure 6 b and d). The measured region of rotor #1 depicts half of the slipstream for both rotating speeds. The vertical velocity colour map, together with the streamtraces, provides an overview of the flow field behaviour. The

Presented at 49th European Rotorcraft Forum, Buckeburg, Germany, 5-7 September, 2023

mean velocity shows the typical wake contraction immediately downstream of the rotor disk reaching a radial position of about x = 0.8 R at an axial distance of z = -0.4 R. A flow acceleration is present down to z = -1 R where the maximum value is reached while moving further downstream the velocity peak remains almost constant as shown in Figure 7-b. The diagram illustrates that the vertical velocity peaks from z = -0.2 R to z = -1.0 R move inward the slipstream while the velocity slopes in the shear layer region decrease moving downward in agreement with the flow diffusion. The mass flow entrainment from the external undisturbed region is described by the streamlines, which in the region contained between the rotor disc and the plane z= -0.4 R shows an upstream flow direction due to the shedding of the tip vortices while downstream the stream tracers bend down entering into the rotor slipstream.

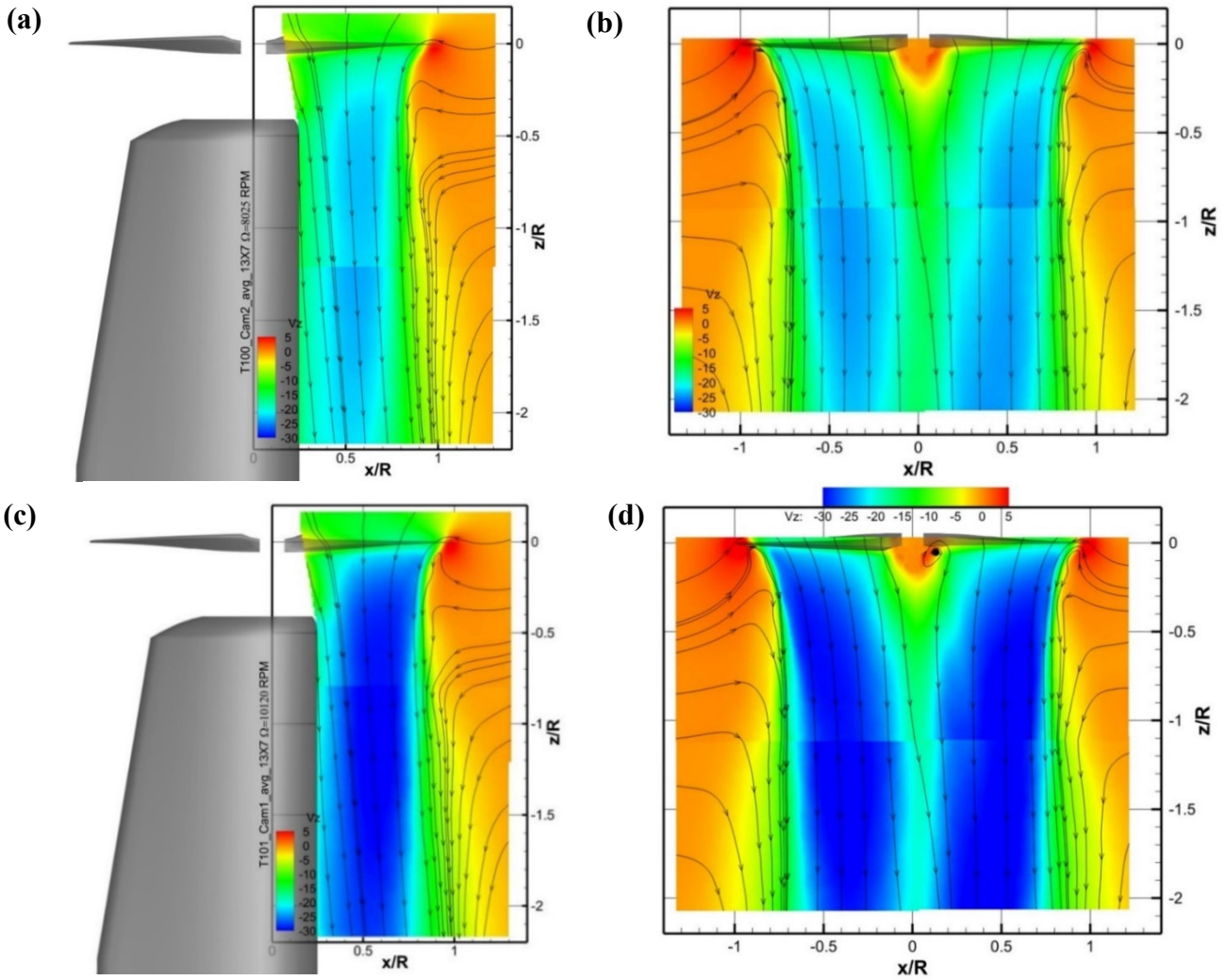

Figure 6: Iso-contours with streamtraces of the ensemble-average flow field colour-coded with the velocity vertical component at Ω = 8025 RPM for rotor #1 (a) and rotor #2 (b) and at Ω = 10120 RPM for rotor #1 (c) and rotor #2 (d)

Presented at 49th European Rotorcraft Forum, Buckeburg, Germany, 5-7 September, 2023

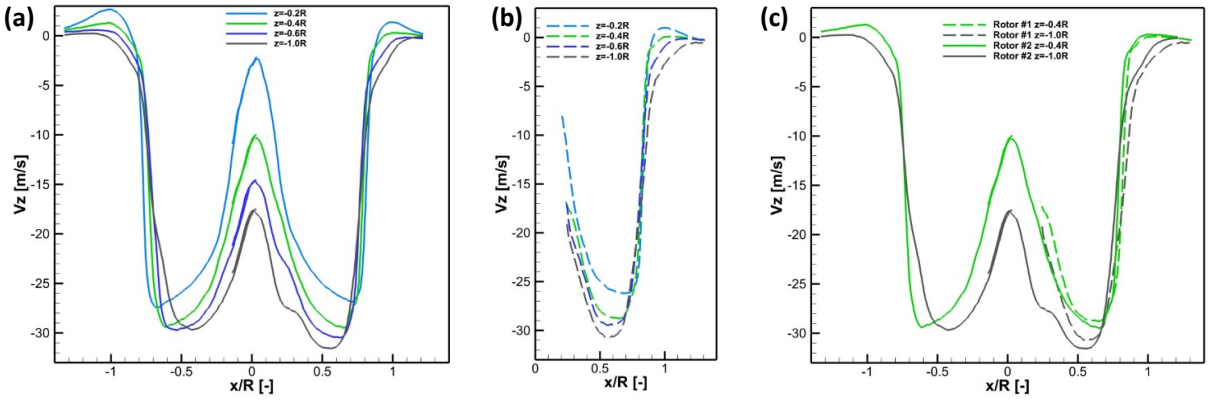

Isolated rotor #2 Isolated rotor #1 Rotor #2 vs Rotor #1

Figure 7: Vertical velocity trend along radial distance at Ω = 10120 RPM for different z-stations (z = -0.4 R, -0.5 R, -0.6 R and -1.0 R): Isolated rotor #2 (a), isolated rotor #1 (b) and Rotor #2 Vs #1 comparison (c)

The rotor #2 slipstream is free to develop downstream as shown in Figure 6-b and Figure 6-d. A similar contraction region is present between the rotor disk and the horizontal plane at a distance of z = -0.4 R with a wake contraction of about x = 0.8 R. The vertical velocity still accelerates also downstream of the contraction region, down to z = -1.0 R as shown in Figure 7-a. It is worth noting that rotor #2 slipstream covers a larger flow region and has higher vertical velocities of about 3% with respect to rotor #1 (Figure 7-c) to support the results of the load measures with rotor #2 thrust and torque higher than rotor #1. Furthermore, rotor #2 vertical velocity at z = -1 R is higher than at z = -0.5 R in the absolute value supporting the higher loss of thrust of rotor #1 at z = -1 R than at z=-0.5 R for the coaxial configuration as shown in Figure 5-a. It is also interesting to notice, that the flow entrainment in the rotor #2 slipstream, presents a small asymmetry, and the streamlines on the right region present a larger upwash concerning the left side.

The wake interaction for coaxial configuration was investigated acquiring for each case 500 instantaneous velocity fields with rotor #2 free to rotate and the PIV measurement phase locked to rotor #1 azimuth position of $\Psi = 90°$ avoiding the spurious vector noise due to the blade passage in the measurement region. The recording procedure considers that the upper region below rotor #2 is not influenced by any particular blade azimuth position, while the flow field from the position of rotor #1 and downstream is affected by the upper slipstream and by the phase-locked flow pattern of the rotor #1.

The ensemble average velocity fields, for the coaxial configuration of Δx = 0 and Δz = -0.5 R for rotating speeds of Ω = 8025 RPM and Ω = 10120 RPM are depicted in Figure 8-a and Figure 8-b. For the sake of brevity, the case at the highest rotating speed is discussed. The mean velocity field shows immediately downstream the rotor #2 position the same contraction of the isolated rotor and a strong acceleration of the vertical velocity. Comparing the velocity trends of coaxial configuration with the isolated rotor #2 at z = -0.4 R and z = -0.5 R, indicates a velocity peak percentage increment of 11.2 % and 15.6 %, respectively (Figure 9 a and b). The coaxial velocities at the stations of z = -0.6 R and z = -1 R are compared with the isolated rotor #1 at x = -0.1 R and x = -0.5R (Figure 9 c and d). The diagram shows a significant increase in the coaxial velocity in terms of 48% and 37% due to the contribution of the upper rotor. The streamlines indicate the presence of two tip vortices released by rotor #1. The vortices, released by blades #1 and #2, have a vortex age of $\Psi_{v1} = 90°$ and $\Psi_{v2} = 270°$, respectively.

The mean velocity field of the coaxial configuration with Δx = 0 and Δz = -1.0 R for rotating speeds of Ω = 8025 RPM and Ω = 10120 RPM are depicted in Figure 8-c and Figure 8-d. The behaviour of the flow field in the region comprised between the two rotors is fairly equivalent to the slipstream of the isolated rotor #2. The vertical velocity of the coaxial configuration at z= -0.4, -0.5 and 0.6 R is slightly larger than 2% of the isolated rotor #2 (Figure 10 a, b and c). At rotor #1 position, at z = -1.0 R, the coaxial vertical velocity is 13% higher than the isolated rotor #2 (Figure 10-d). In addition, the coaxial vertical velocity at z = -1.15 R is compared with the isolated rotor #2 at z = -1.15 R and with rotor #1 at z = -0.15 R (Figure 11). The wake interference induces an increment of the vertical peak velocity of 45 % and 21.8% concerning rotors #2 and #1, respectively.

Presented at 49th European Rotorcraft Forum, Buckeburg, Germany, 5-7 September, 2023

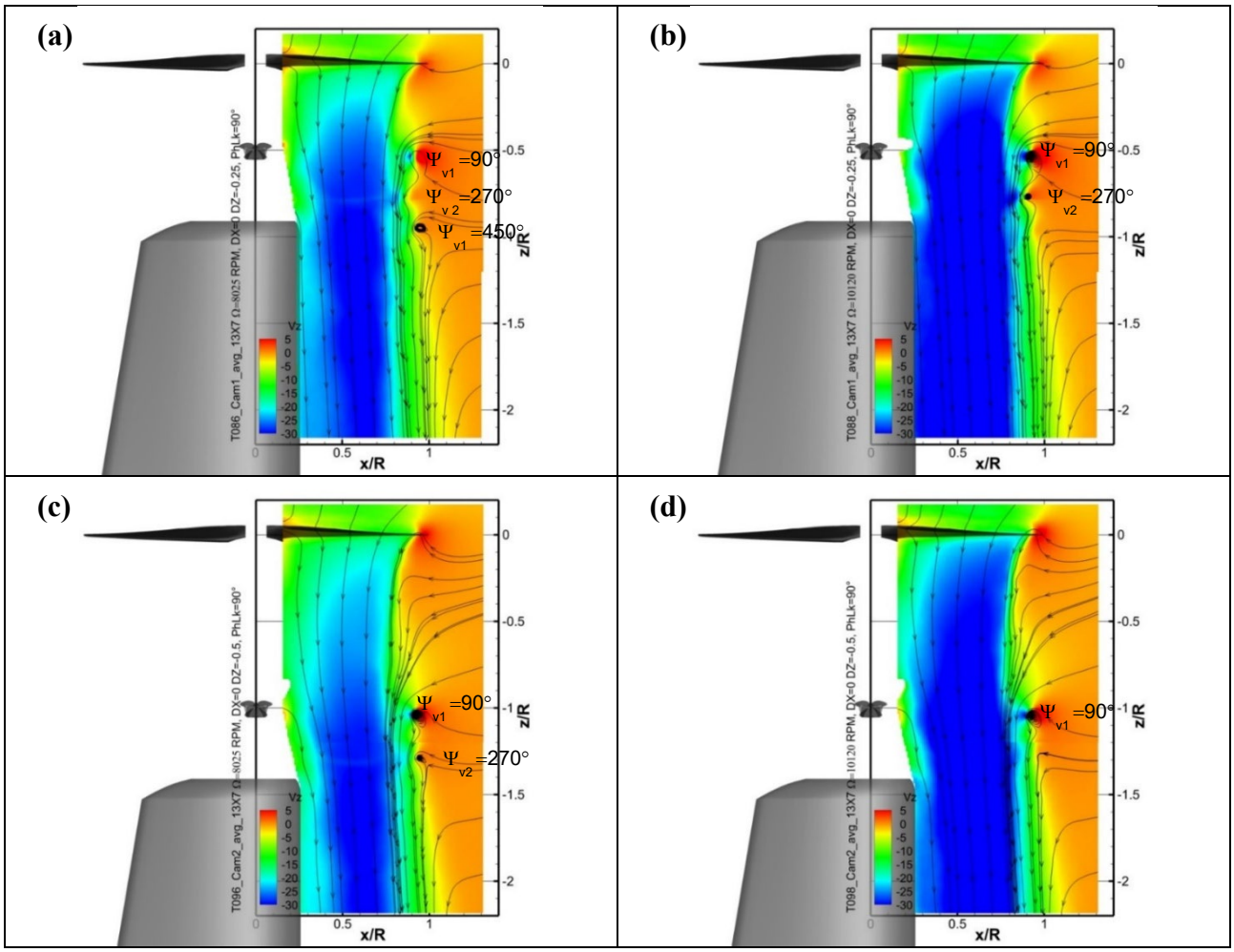

Figure 8: Iso-contours with stream-traces of the ensemble-average flow field colour-coded of the vertical component of the velocity for the coaxial configuration with Δz = 0.5 R at Ω = 8025 RPM (a) and Ω = 10120 RPM (b) and for coaxial configuration with Δz = 1.0 R at Ω = 8025 RPM (c) and Ω = 10120 RPM (d)

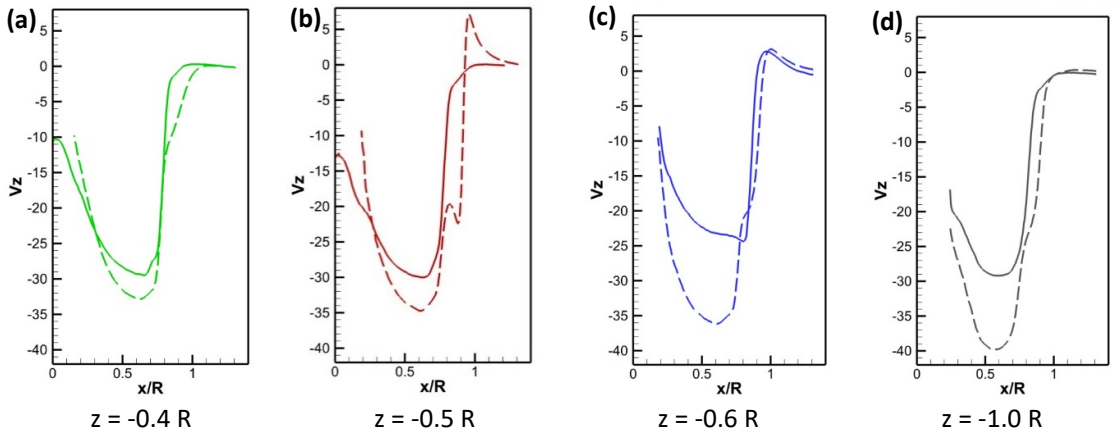

Figure 9: Comparison between vertical velocity path along the radial direction of the single rotor (solid lines) and coaxial configuration with Δx = 0 and Δz = 0.5 R (dashed line) at different vertical positions z = -0.4 R (a), z = -0.5 R (b), z = -0.6 R (c) and z = -1.0 R (d) for a rotating speed of Ω = 10120 RPM.

Presented at 49th European Rotorcraft Forum, Buckeburg, Germany, 5-7 September, 2023

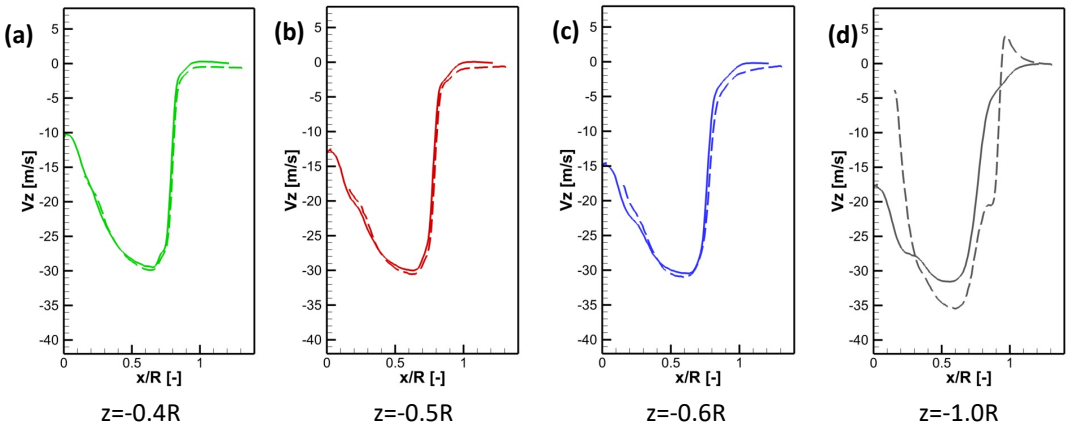

Figure 10: Vertical velocity distributions along the radial direction of single rotors (solid lines) and coaxial configuration with Δx = 0 and Δz = 1.0 R (dashed line) at different vertical positions z = - 0.4 R (a), z = -0.5 R (b), z = -0.6 R (c) and z = -1.0 R (d) for a rotating speed of Ω = 10120 RPM.

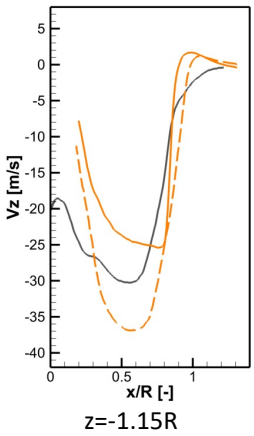

Figure 11: Vertical velocity vs radial distance normalized by the rotor radius for isolated rotor #2 at z = -1.15 R (grey solid line), rotor #1 at z = -0.15 R (orange solid line) and coaxial configuration with Δx = 0 and Δz = -1.0 R at z = -1.15 R (orange dashed line)

4.3 Phase-locked flow Fields

PIV measurements phase-locked with rotor azimuth angle positions were performed to investigate the tip vortices positions and characteristics of the isolated rotors for both rotating speeds. The slipstream was investigated for different rotor azimuthal positions ranging from $\psi = 0°$ to $\psi = 270°$ with a step incremental of $\Delta\psi = 30°$. For each azimuthal angle, 50 instantaneous velocity fields were recorded. The phase-locked mean velocity field was obtained by averaging the complete set of data. For example, the out-of-plane vorticity (ω_y) of the mean flow field recorded at $\psi = 60°$ is shown in Figure 12 for both rotors. The rotor #1 vorticity map depicts the presence of the tip vortices as intense concentrated counter-clockwise vorticity, (red spots in Figure 12-a) distributed along the slipstream shear layer together with the trailing edge vorticity strips. Wake age (ζ_i) and tip vortex age (ψ_{vi}) are indicated on the plot with the respective ith blade they belong to. The vortices shed by the blade root present a clockwise rotating versus and they appear as blue spots accompanied by the trailing edge vorticity stripe. Figure 12-a shows in the upper region the blade #1 tip vortex characterized by a vortex age of $\psi_{v1} = 60°$. The vortex is linked to the root vortex by the trailing edge vorticity sheet which crosses the entire slipstream. Immediately downstream and inward of the slipstream, the tip vortex shed by blade #2 ($\psi_{v2} = 240°$) is present without any additional vortical structures. Further downstream the vorticity sheet released by the second blade ($\zeta_2 = 240°$) is connected to the blade #1 tip vortex with vortex age of $\psi_v = 420°$ due to the higher downwash speed inside the slipstream in agreement with the work of Martin and Leishman [12]. The vortex age indicates that after the second revolution, a roll-up of the tip vortices occurs presenting the older vortex ($\psi_{v2} = 960°$) above the younger vortex ($\psi_{v1} = 780°$).

Rotor #2 presents the full slipstream vorticity colour map. Both the blade tip and root vortices are depicted together with the trailing edge vorticity stripes. A vortex distribution similar to that of rotor #1 is identified in Figure 12-b. The detection of the centre position of the tip vortices has been performed using

Presented at 49th European Rotorcraft Forum, Buckeburg, Germany, 5-7 September, 2023

the Γ_2 criterion proposed by Graftieaux et al. [13], a criterion that has been assessed and selected for the typology of the current data [14].

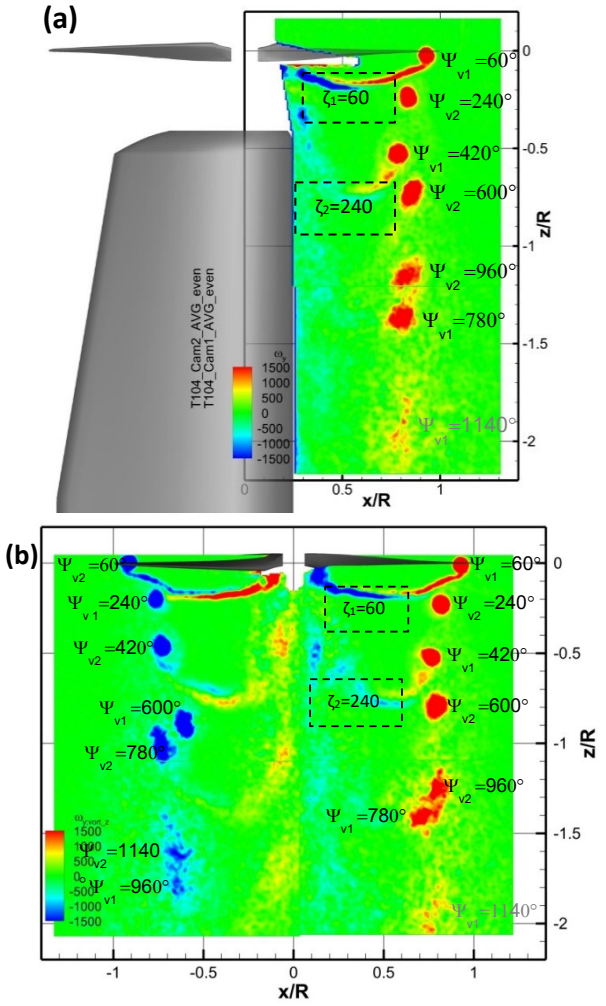

Figure 12: Iso-contours of the mean phase-locked velocity field colour-coded with the out-of-plane vorticity component at Ω = 10120 RPM for rotor #1 (a) and rotor #2 (b)

The out-of-plane vorticity colour maps of the ensemble average velocity field for both isolated rotors are depicted in Figure 13. In addition, the positions of the vortex centres of each mean phase-locked velocity field are overlapped. The rotor slipstream boundary is characterised by a region of intense vorticity due to the passage of the tip vortices and by the presence of a strong velocity gradient in the shear layer. The slipstream boundary presents the typical radial contraction immediately below the rotor disk reaching the position of $x = 0.8R$ at $z = -0.2R$ and then continuing almost constant down to about $z = -0.6R$ where the vortex trajectory splits and then re-joins downstream at about $z = -1.3R$. For rotor #1 only half of the slipstream is measured (Figure 13-a) while the full slipstream of rotor #2 is available in Figure 13-b. The vorticity and vortex path for rotor #2 present a slight asymmetry. The trajectory of the vortices detaching by the left blade anticipates the path bifurcation concerning the right blade path. Rotor #2 tip vortices shedding from the root blades have a longer path with respect to that of rotor #1 due to the missing obstacles.

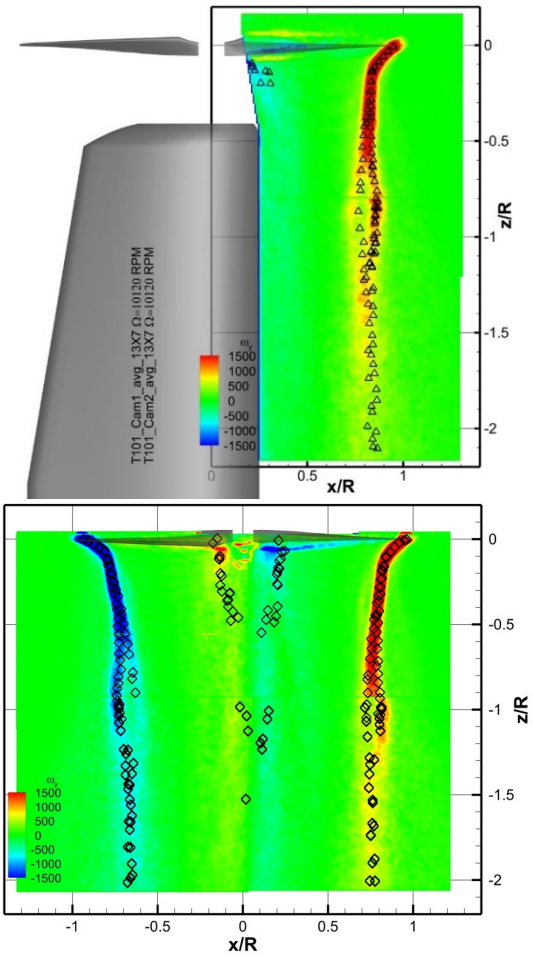

Figure 13: Out-of-plane vorticity colour map of the ensemble average velocity field with the collection of the vortex centres positions of all the mean phase-locked velocity fields, rotor #1 (a) and rotor #2 (b).

4.4 Acoustic field

In this section, the acoustic data from the AWB measurement campaign discussed earlier are presented and related to the findings of the flow field measurements. We consider the coaxial rotor configuration with counter rotating blades as shown in Figure 14, for variations in rotor spacing. The upper rotor (rotor #2 as mentioned in the previous section) is a left-handed rotor with a clockwise rotation direction and the lower rotor (rotor #1) is a right-handed rotor with a counter-clockwise rotation direction. We consider fixed microphone positions at $\theta = 0°, -15°$ and $-30°$ relative to the lower rotor plane of rotation and a distance $r = 1.82\ R$ away from the hub's origin as defined in Figure 14. This analysis will allow an evaluation of the effect of the proximity

Presented at 49th European Rotorcraft Forum, Buckeburg, Germany, 5-7 September, 2023

of the upper rotor to the lower one on the acoustic radiation.

The acoustic results are presented in Figure 15, for 10.000 RPM. Narrow-band sound pressure level (SPL) spectra obtained through spectral averaging of individual data blocks are presented in Figure 15-a. Conversely, narrow-band SPL spectra obtained through temporal averaging of individual data blocks are presented in Figure 15-b. The spectral bandwidth of the analysis is $\Delta f = 5.22$ Hz. The data analysis is performed with the rotors operated in a random phase, as no means to control their relative phase was available in the experiment. In the graphs of Figure 15, each row corresponds to a specific microphone position, or radiation angle relative to the lower rotor plane. The comparison at $\theta = -30°$ also includes data at $\theta = -39°$ for configuration $\Delta z = 0.5\,R$ as no data at $\theta = -30°$ was available for this configuration.

The results of Figure 15-a reveal an increased tonal and broadband noise in the coaxial configuration than that observed for the isolated rotor case. Both tonal (harmonic and sub-harmonic) and broadband noise are found to increase as the rotor spacing increases. At $\theta = 0°$ and $\theta = -15°$, the first three harmonics, i.e. BPF = 1, 2, 3, are not affected by a change in rotor spacing, whereas for $\theta = -30°$ only the second and third harmonics are sensible to the rotor spacing. The effect of rotor spacing on tonal acoustics is emphasized by averaging the data in the time domain, e.g. Figure 15-b. Time domain averaging removes contributions to the spectrum due to stochastic sources of sound, i.e. broadband leading-edge, trailing-edge and tip interaction noise.

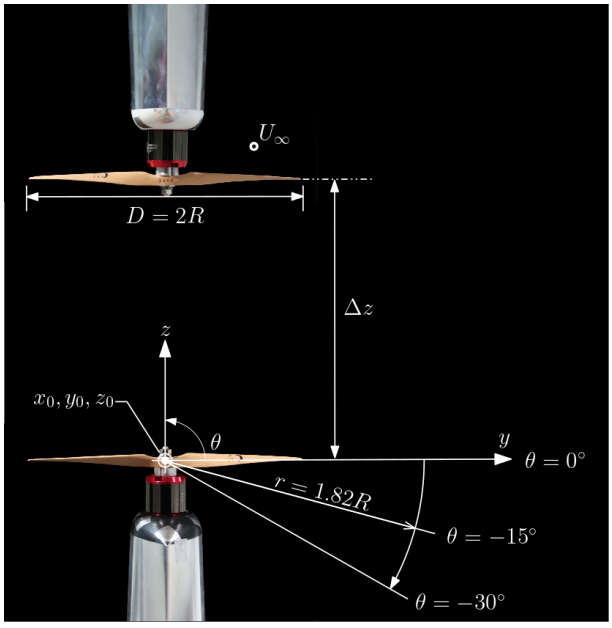

Figure 14: Coordinates system definition for the presentation of the acoustic data

The observed SPL increase is somewhat counter-intuitive but consistent with the experimental observations of Paruchuri et al. [15] and Mcthane et al. [16] as well as with the calculations of Blandeau et al. [17]. Noteworthy is that, at all three microphone positions considered in Figure 15, the first harmonic is not affected by rotor spacing changes. The SPL of the first harmonic is a function of rotor averaged thrust and it was verified that a change in rotor spacing only has a minor impact on the rotor's thrust, as proven in Figure 16. Hence, Figure 16 shows the impact of the vertical distance between the rotors in coaxial configuration Δz on the thrust with respect to that evaluated at $\Delta z = 2R$ for both rotors. The upper rotor is subjected to roughly 1 % loss in thrust, whereas the lower rotor experiences a rough 3% gain at $\Delta z = R/2$ relative to the $\Delta z = 2R$ configuration's thrust values. The strong sub-harmonics components identified in the isolated rotor configuration were already assigned to slight geometric differences in the rotor's blades as well as the contribution of the motor noise [5]. Increased sub-harmonic levels in the coaxial configuration suggest that the ingestion of the incoming unsymmetrical turbulent vortex flow field from the upper rotor by the lower rotor further escalates the effect of the blade's geometry variations. This, in turn, makes worse the unsteady loading of the rotor's blades leading edge. Therefore, this implies that rotor #1 (lower rotor) drives the sub-harmonic's increase because rotor #2 (upper rotor) is not subjected to a disturbed inflow. The broadband SPL increment, observed in Figure 15, is the consequence of the interaction of the disturbed inflow, due to the mixed wakes. Firstly, the upper rotor's mean wake velocity increases with the vertical distance between each other, e.g. Figure 7-a,c. In addition, the PIV measurements confirm that increasing the rotor spacing leads to higher levels of turbulence kinetic energy (TKE), e.g. Figure 17. The high TKE intensity in the wake shear layer region, i.e. $0.5 < x/R < 1.0$, is observed to spread wider for the $\Delta z = 1.0R$ case compared to the $\Delta z = 0.5\,R$ case. Thus, a wider part of the blade will interact with the high-intensity part of the incoming turbulent flow, potentially resulting in increased sound production. Further support for this hypothesis is provided in Figure 18. In this figure, the vortex centre locations from 110 individual PIV snapshots are presented for cases $\Delta z = 0.5\,R$ (Figure 18-a) and $\Delta z = 1.0\,R$ (Figure 18-b). The results of Figure 18 clearly show a wider spatial spreading in x and z of the instantaneous vortex centre positions at $\psi_v = 90°$ for the $\Delta z = 1.0R$ case compared to the $\Delta z = 0.5R$ case. The vortex meandering for the $\Delta z = 1.0R$ case is 150% larger than that at the closer distance along the x- direction and 15% along the z-axis. The more pronounced spatial spreading of the tip vortices is indicative of important unsteadiness in the flow field, especially towards the blade tip region where a higher

Presented at 49th European Rotorcraft Forum, Buckeburg, Germany, 5-7 September, 2023

Mach number occurs and therefore higher extra noise is expected. Also, due to the larger spatial extent of the high-intensity TKE regions, one could expect a shift towards a lower frequency of the broadband noise spectral maximum. The spectra of Figure 15a support this hypothesis, especially when considering the cases $\Delta z = R$ and $\Delta z = 2R$.

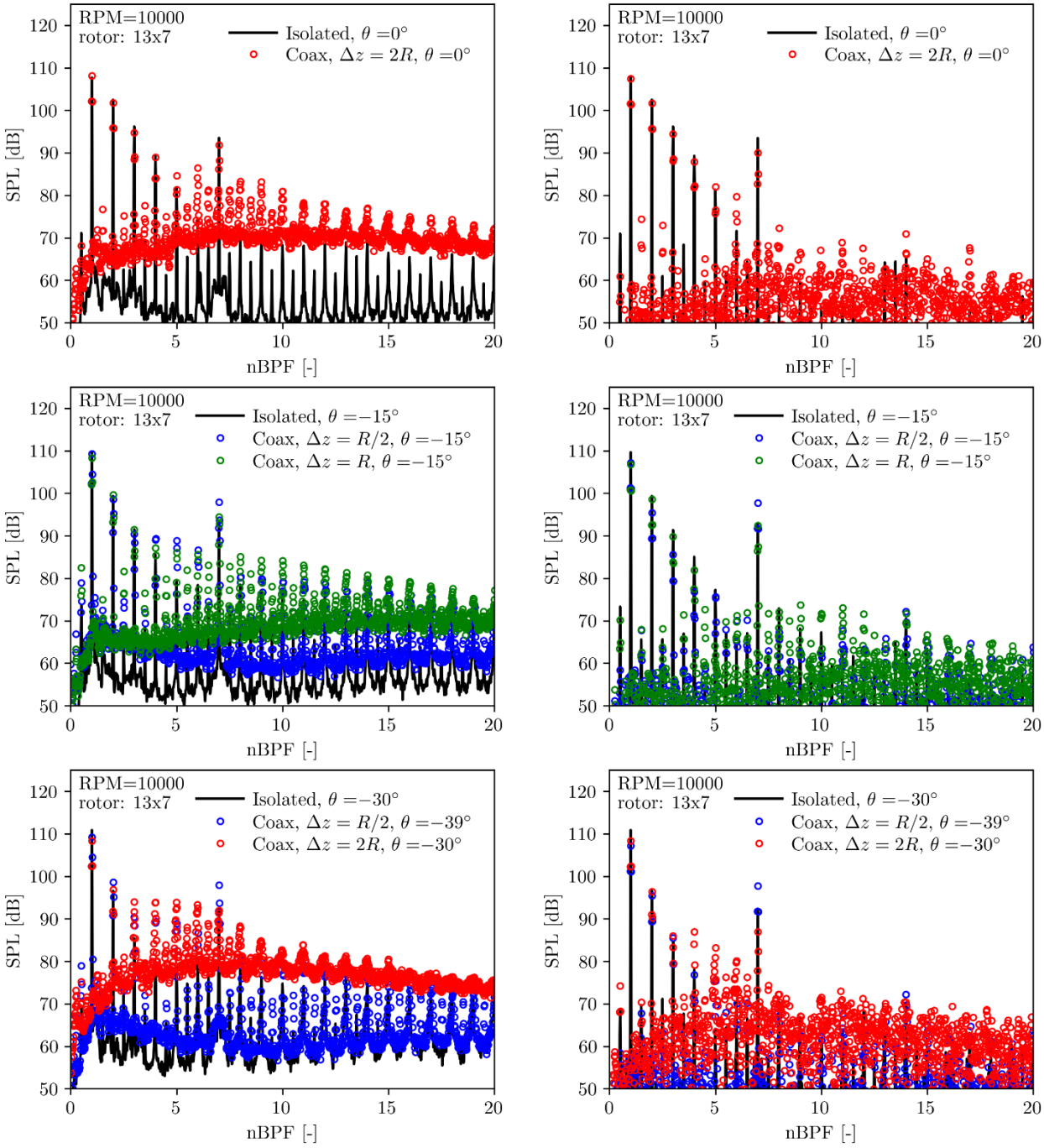

(a) Spectral averaged data

(b) Time averaged data

Figure 15: Acoustic emissions vs coaxial rotor separation and radiation direction. Left, spectral averaged data. Right, time averaged data. Spectral analysis bandwidth; $\Delta f = 5.22$ Hz.

Presented at 49th European Rotorcraft Forum, Buckeburg, Germany, 5-7 September, 2023

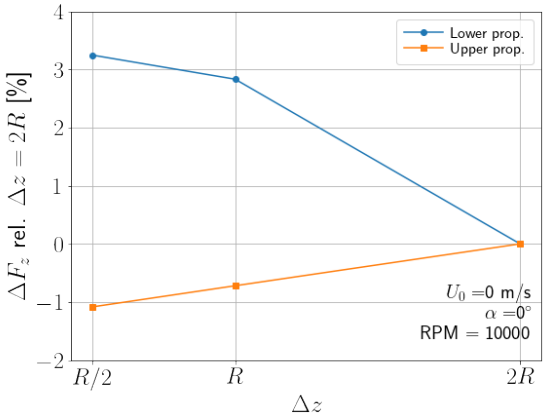

Figure 16: Coaxial configuration, the relative change in thrust vs. rotor spacing.

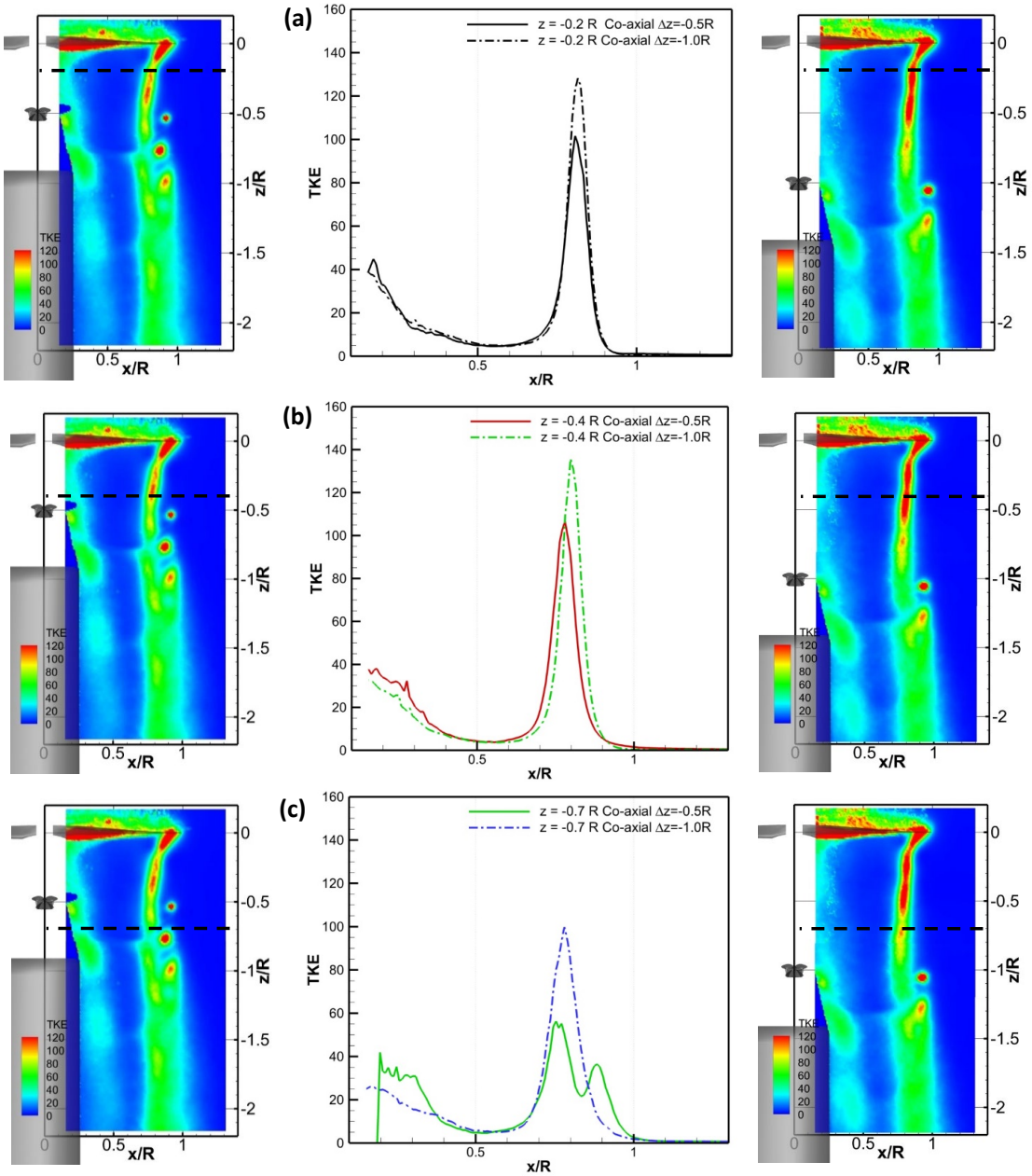

Figure 17: TKE colour map for coaxial configurations $\boldsymbol{\Delta z = 0.5R}$ (left side) and $\boldsymbol{\Delta z = 1.0\,R}$ (right side). TKE radial distribution (center) at $z = -0.2R$ (a) $z = -0.4R$ (b) $z = -0.7R$ (c)

Presented at 49th European Rotorcraft Forum, Buckeburg, Germany, 5-7 September, 2023

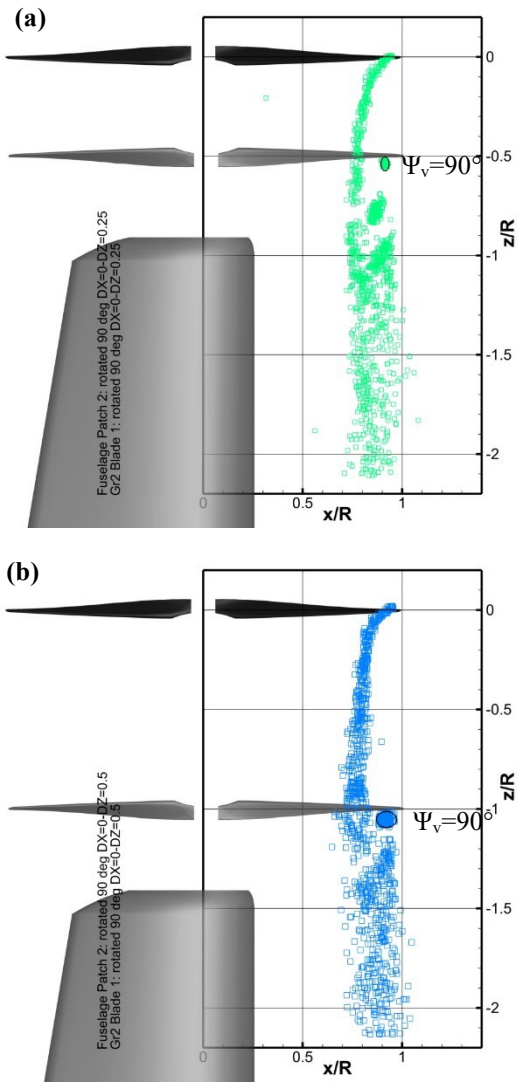

Figure 18: Vortex path as extracted from 110 individual PIV snapshots for $\Delta z = 0.5R$ (a) and $\Delta z = 1.0R$ (b)

5 CONCLUSIONS

Experimental investigations of isolated and coaxial rotors have been carried out at DLR Acoustic Wind Tunnel and subsequently at CIRA laboratories. The first test was aimed at acoustic characterization while the second entry was focused on the fluid dynamic investigation. Both campaigns have foreseen rotor load measurements, assuring the correct repeatability. The effect of the support on the isolated rotor performance was assessed showing that the rotor with a slipstream free to evolve without the presence of the pylon presented higher values of the thrust and torque with respect to the rotor supported from below. The aerodynamic behaviour is supported by the PIV results which elucidate higher values of the induced velocity and momentum for the case of the rotor with unobstructed slipstream. The coaxial configuration presents negligible effects on the performance of the upper rotor while the lower one is affected by a marked loss of the thrust and a small increment of the torque due to the incoming slipstream. The inspection of the acoustic emissions reveals an increased tonal and broadband noise in the coaxial configuration concerning that observed for the isolated rotor case. The increment of the rotor distance produces a thrust loss and a growth of the tonal (harmonic and sub-harmonic) and broadband noise. The acoustics results are supported by the increment of the TKE value and by the larger meandering of the tip vortex.

6 REFERENCES

[1] Straubinger, A., Rothfeld, R., Shamiyeh, M., Büchter, K.-D., Kaiser, J., and Plötner, K. O., “An overview of current research and developments in urban air mobility–Setting the scene for UAM introduction,” Journal of Air Transport Management, Vol. 87, 2020, p. 101852.

[2] Johnson, W., and Silva, C., “NASA concept vehicles and the engineering of advanced air mobility aircraft,” The Aeronautical Journal, Vol. 126, No. 1295, 2022, pp. 59–91.

[3] Yin, J., De Gregorio, F., Petrosino, F., Rossignol, K-S, Schwarz, T., Cotte, B., Brouwer, H., Clero, F., Mortain, F., Reboul, G., Zanotti, A., Vigevano, L., Gibertini, G., Bernardini, G. Schmähl, M., Kaltenbach, H-K., Pagliaroli, T., Keßler, M., Barakos, G., Ragni, D., Testa, C.: Noise Radiation and Propagation for Multirotor System Configurations. In: Terms of Reference for the GARTEUR Action Group HC/AG-26, December 2021.

[4] Rossignol, K.-S., Yin, J., Rottmann, L., “Investigation of Small-Scale Rotor Aeroacoustic in DLR's Acoustic Wind Tunnel Braunschweig,” in 28th AIAA/CEAS Aeroacoustics 2022 Conference., Southampton, UK, 2022

[5] Yin, J., Rossignol, K.-S., Rottmann, L., Schwarz, T.: Numerical Investigations on Small-scale Rotor Configurations with Validation using Acoustic Wind Tunnel Data. In: 48th European Rotorcraft Forum (ERF), 2022, Seiten 1-17. 48 European Rotorcraft Forum (ERF) 2022, 6.- 8. September 2022, Winterthur, Switzerland.

[6] Nargi, R.E., De Gregorio, F., Candeloro, P., Ceglia, G. and Pagliaroli T., “Evolution of flow structures in twin-rotors wakes in drones by time-resolved PIV,” Journal of Physics: Conference Series, Vol. 1977, 2021, pp. 012008.

Presented at 49th European Rotorcraft Forum, Buckeburg, Germany, 5-7 September, 2023

[7] Ceglia, G., Nargi R.E., Candeloro P., Pagliaroli, T., De Gregorio, F., "Time-resolved PIV measurements of the rotor wake in a side-by-side configuration" 15th International Symposium on Particle Image Velocimetry, San Diego, CA, June 2023.

[8] Zanotti, A. and Algarotti, D., "Aerodynamic interaction between tandem overlapping propellers in eVTOL airplane mode flight condition," Aerospace Science and Technology 124: 107518, 2022.

[9] Pott-Pollenske, M., and Delfs, J., "Enhanced capabilities of the aeroacoustic wind tunnel Braunschweig," 14th AIAA/CEAS Aeroacoustics Conference (29th AIAA Aeroacoustics Conference), 2008, p. 2910.

[10] Yin, J., De Gregorio F., et al "Acoustic and Aerodynamic Evaluation of DLR Small-Scale Rotor Configurations within GARTEUR AG26", 49th European Rotorcraft Forum, September 5 – 7, 2023, Bückeburg, Germany.

[11] Raffel M., Willert C. E., Wereley S. T., and Kompenhans J. (2007) Particle Image Velocimetry - A Practical Guide, Springer-Verlag Berlin Heidelberg, 2nd edition doi: 10.1007/978-3-540-72308-0.

[12] Martin, B.M. and Leishman, J.B., "Trailing vortex measurements in the wake of a hovering rotor blade with various tip shapes," 58th Annual Forum of the AHS International, Montreal, Canada, June 11-13, 2002.

[13] Graftieaux L., Michard M. and Grosjean N. (2001) Combining PIV, POD and vortex identification algorithms for the study of unsteady turbulent swirling flows. Meas. Sci. Technol. 12 1422–1429.

[14] De Gregorio F., Visingardi A. (2020) Vortex detection criteria assessment for PIV data in rotorcraft applications. Exp Fluids 61, 179. doi:10.1007/s00348-020-03012-7.

[15] Paruchuri C., Joseph P., Prior S. and Parry, A.B. (2022) On the optimum separation distance for minimum noise of contra-rotating rotors. Journal of Sound and Vibration, 535, p.117032. doi:10.1016/j.jsv.2022.117032

[16] Mcthane E., Zahirudin R. A. R., Hafner A., Greenwood E. and Palacios J., Effects of Varying Separation Distance on the Acoustics and Performance of Counter-Rotating Coaxial Rotors. AVIATION Forum 2023, San Diego, USA, AIAA 2023-4292, doi:10.2514/6.2023-4292

[17] Blandeau V. P. and Joseph P. F., Broadband Noise Due to Rotor-Wake/Rotor Interaction in Contra-Rotating Open Rotors, AIAA Journal, Vol. 48, No. 11, November 2010, doi: 10.2514/1.J050566